The Astrophysical Journal, 971:107 (14pp), 2024 August 10 https://doi.org/10.3847/1538-4357/ad5445

Detection of a Spatially Extended Stellar Population in M33: A Shallow Stellar Halo?

Itsuki Ogami[1,2], Yutaka Komiyama[3], Masashi Chiba[4], Mikito Tanaka[3], Puragra Guhathakurta[5], Evan N. Kirby[6], Rosemary F. G. Wyse[7], Carrie Filion[7], Takanobu Kirihara[8], Miho N. Ishigaki[2], and Kohei Hayashi[4,9,10]
[1] The Graduate University for Advanced Studies (SOKENDAI), 2-21-1 Osawa, Mitaka, Tokyo 181-8588, Japan; itsuki.ogami@grad.nao.ac.jp
[2] National Astronomical Observatory of Japan, 2-21-1 Osawa, Mitaka, Tokyo 181-8588, Japan
[3] Department of Advanced Sciences, Faculty of Science and Engineering, Hosei University, 3-7-2 Kajino-cho, Koganei, Tokyo 184-8584, Japan
[4] Astronomical Institute, Tohoku University, Aoba-ku, Sendai, Miyagi 980-8578, Japan
[5] Department of Astronomy and Astrophysics, University of California Santa Cruz, University of California Observatories, 1156 High Street, Santa Cruz, CA 95064, USA
[6] Department of Physics and Astronomy, University of Notre Dame, Notre Dame, IN 46556, USA
[7] Department of Physics and Astronomy, Johns Hopkins University, Baltimore, MD 21218, USA
[8] Kitami Institute of Technology, 165, Koen-cho, Kitami, Hokkaido 090-8507, Japan
[9] National Institute of Technology, Sendai College, Natori, Miyagi 981-1239, Japan
[10] Institute for Cosmic Ray Research, The University of Tokyo, Kashiwa, Chiba 277-8582, Japan
Received 2024 March 22; revised 2024 May 9; accepted 2024 June 3; published 2024 August 8

Abstract

We analyze the outer regions of M33, beyond 15 kpc in projected distance from its center, using Subaru/Hyper Suprime-Cam multicolor imaging. We identify red giant branch (RGB) stars and red clump (RC) stars using the surface-gravity-sensitive *NB515* filter for the RGB sample and a multicolor selection for both samples. We construct the radial surface density profiles of these RGB and RC stars and find that M33 has an extended stellar population with a shallow power-law index of $\alpha > -3$, depending on the intensity of the contamination. This result represents a flatter profile than the stellar halo that was detected by the previous study focusing on the central region, suggesting that M33 may have a double-structured halo component, i.e., inner/outer halos or a very extended disk. Also, the slope of this extended component is shallower than those typically found for halos in large galaxies, implying intermediate-mass galaxies may have different formation mechanisms (e.g., tidal interaction) from large spirals. We also analyze the radial color profiles of RC/RGB stars and detect a radial gradient, consistent with the presence of an old and/or metal-poor population in the outer region of M33, thereby supporting our proposal that the stellar halo extends beyond 15 kpc. Finally, we estimate that the surface brightness of this extended component is $\mu_V = 35.72 \pm 0.08$ mag arcsec^{-2}. If our detected component is the stellar halo, this estimated value is consistent with the detection limit of previous observations.

Unified Astronomy Thesaurus concepts: Triangulum Galaxy (1712); Galaxy stellar halos (598); Local Group (929)

1. Introduction

In the Λ-dominated cold dark matter scenario, mergers play an important role in galaxy formation. The way in which galaxies build their mass depends mostly on this process (Bullock & Johnston 2005). After an accretion event, accreted stars are distributed in the outer region of a galaxy as a diffuse and dynamically distinct component, which is called a stellar halo. This extended stellar component is thus important for understanding the accretion history of a galaxy.

Observations of stellar halos of disk galaxies and studies of their properties have been limited to nearby large galaxies such as the Milky Way and M31. In the Milky Way, the nature of the stellar halo has been explored by wide-field surveys such as the Sloan Digital Sky Survey (York et al. 2000), Pan-STARRS (Chambers et al. 2016), the Dark Energy Survey (Abbott et al. 2018), the Gaia mission (Gaia Collaboration et al. 2016), HSC-SSP (Aihara et al. 2018a), and so on. Thanks to these surveys, it has been shown that the Milky Way's stellar halo is characterized by dual global halo structures (e.g., Carollo et al. 2007; Fukushima et al. 2018). In particular, many observations have found that the inner halo profile of the Milky Way shows a shallow power-law profile with $\alpha \sim -3$ (e.g., Jurić et al. 2008), while its outer halo profile is represented as a steep profile with $\alpha \sim -6$ for the Galactocentric radius of $50 \lesssim r \lesssim 100$ kpc (Deason et al. 2014) and again shows a shallow profile with $\alpha = -3.2 \sim -4.0$ at $100 \lesssim r \lesssim 200$ kpc (e.g., Thomas et al. 2018; Fukushima et al. 2019). Comparison to cosmological simulations suggests that the steep profile beyond $r \sim 50$ kpc indicates that the Milky Way has experienced a relatively quiet accretion history over the past few gigayears (Deason et al. 2014). Besides this, these surveys have also increased the number of newly identified satellite galaxies and substructures (e.g., Homma et al. 2016, 2024; Suzuki et al. 2024). In M31, the Pan-Andromeda Archaeological Survey (PAndAS; McConnachie et al. 2009) and the SPLASH survey (Gilbert et al. 2009) have shown that its halo has a power-law surface brightness profile (e.g., Ibata et al. 2014) and extends to 175 kpc (Gilbert et al. 2012). In addition, beyond the Local Group, halos in many large galaxies (e.g., M81, NGC4631, and M101), which are comparable in mass and size to the Milky Way, have been observed (Okamoto et al. 2015; Tanaka et al. 2017; Jang et al. 2020). However, for smaller galaxies such as M33, few observations have been conducted to probe the nature of the stellar halo, due to its faintness.

M33 is a dwarf spiral galaxy located 859 kpc from the Sun (de Grijs et al. 2017) and it is a possible satellite of M31. M33 has a stellar mass of $3.2 \times 10^9 M_\odot$ (Van Der Marel et al. 2012)

and a virial mass of $2 \times 10^{11} M_{\odot}$ (Corbelli et al. 2014). Applying the stellar mass–halo mass relation (e.g., Behroozi et al. 2019), M33 should have a stellar halo with a mass of $8 \times 10^{7} M_{\odot}$.

The existence of the M33 halo has been the subject of much debate. PAndAS was unable to detect its stellar halo down to $\mu_V < 35.5$ mag arcsec^{-2} in the region within 3.75° from the center of M33 (McMonigal et al. 2016). In addition, recent narrowband photometry, which was conducted out to a maximum projected distance of about 40 kpc from the center of M33, has failed to detect any planetary nebulae outside the disk, suggesting the absence of a stellar halo (Galera-Rosillo et al. 2018). However, recent spectroscopic observations have revealed a dynamically hot population in the central region of M33, which is different from the disk component (Gilbert et al. 2022). Moreover, Hubble Space Telescope (HST) multicolor imaging (the Panchromatic Hubble Andromeda Treasury: Triangulum Extended Region survey or PHATTER survey) proposed that M33 has a power-law stellar halo with an index of $\alpha \sim -3$ over the projected radius of $R = 5$ kpc from the center of M33 (Smercina et al. 2023). However, the studies that find evidence for a stellar halo in M33 have been limited to the inner region ($R < 5$ kpc), where the disk population dominates (the disk scale length is 1.86 kpc; Kam et al. 2015). So the outer region, which is unique to the stellar halo, including the presence of faint substructures and the detection of the edge of the stellar halo, has not been clarified.

In PAndAS, an extended disk was found in M33, suggesting an interaction between M31 and M33 (McConnachie et al. 2009). It was also confirmed that M33 accounts for 73% of the total stellar mass of M31 satellites (McConnachie et al. 2018). Therefore, the interaction between M31 and M33 would make a significant contribution to the merger history of M31. Ibata et al. (2007) reported that M33 was confirmed as metal-poor and it was initially expected that a stellar halo would be detected in PAndAS. However, statistical modeling of M33 failed to detect the stellar halo plausibly, because the data were too shallow (McMonigal et al. 2016).

To investigate the global properties of the M33 stellar halo, we have been conducting a photometric survey of M33 using the Subaru/Hyper Suprime-Cam (HSC). HSC is an outstanding instrument for the detailed and high-quality detection and characterization of the M33 stellar halo, using the faint red giant branch (RGB), red clump (RC), and horizontal branch stars as tracers. HSC's three broadband filters, the $g/r_2/i_2$ bands, and one narrowband filter, *NB515*, are a good combination for removing contaminants. By combining the three broadband filters, it is possible to remove unresolved background galaxies using color selections. *NB515*, centered on the MgH/Mgb lines, which are sensitive to stellar surface gravity (Majewski et al. 2000), can be used to remove foreground Galactic dwarf stars (Komiyama et al. 2018; Ogami et al. 2024). Therefore, the removal of these contaminants and the wide and deep HSC observations are expected to provide the nature of the faint M33 stellar halo.

In this paper, we report the initial results of the ongoing survey and analyses of the M33 halo using the Subaru/HSC. We focus on the western region of M33, which is perpendicular to the major axis of the disk and is not significantly affected by contamination from the extended disk of M33, to investigate the properties of the stellar halo. From this analysis, we demonstrate the superiority of Subaru/HSC for detecting the faint stellar halo in M33. The paper is organized as follows. In Section 2, we describe our observational data and data reduction using the HSC pipeline. In Section 3, we introduce the method for selecting the halo stars of M33. The results of the radial profiles of M33 are given in Section 4, and the discussion for these results is presented in Section 5. Finally, Section 6 concludes this paper.

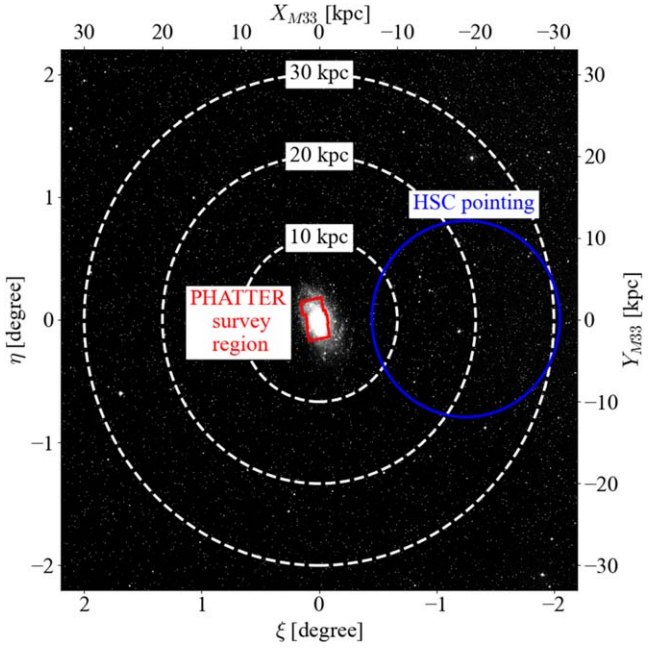

Figure 1. The blue circle indicates the HSC observation field showing a tangent plane centered on M33. The red polygon shows the survey fields observed by the HST (PHATTER survey). The background image is taken from PS1 (Schlafly et al. 2012; Tonry et al. 2012; Magnier et al. 2013; Flewelling et al. 2020).

2. Observation and Data Reduction

We observed the western region of M33 in the g, r_2, and i_2 bands and *NB515* using Subaru/HSC during the nights of 2022 and 2023 (PI: I. Ogami; Proposal IDs: S22B-107 and S23B-072). The observed region is the single pointing, which corresponds to the field of view of HSC ($\sim$1.76 deg^2), shown as the blue circle in Figure 1. In Figure 1, we show the observational fields of the PHATTER survey (Williams et al. 2021; Smercina et al. 2023) as a reference. Our field reaches a projected radius up to $\sim$30 kpc from the center of M33. In this outer region, the disk contamination, which includes the perturbed disk structure (McConnachie et al. 2009), is relatively low, because this region is perpendicular to the major axis of the M33 disk and the orientation of the extended disk, so we can focus on the presence of the stellar halo. Our observations were carried out under relatively good seeing conditions (0.″50–1.″1).

The observed raw images are processed and calibrated using the HSC pipeline (hscPipe version 8.4; Bosch et al. 2018). The hscPipe is based on software for the Large Synoptic Survey Telescope (Ivezic et al. 2008) project. The hscPipe conducts data reduction, including bias and dark subtraction, flat-fielding, sky subtraction, and cosmic-ray removal. After the reduction for individual CCDs, this pipeline calibrates the coordinates and flux scales using Pan-STARRS1 (PS1; Schlafly et al. 2012; Tonry et al. 2012; Magnier et al. 2013;

Table 1
The Details of Our Observations

Band	Date (mm/yyyy)	Exposure Time (s)	Seeing FWHM (arcsec)	50% Detection Completeness Magnitude (mag)
g band	10/2022	$60 \times 5 + 300 \times 15$	0.54 ± 0.03	26.63
r_2 band	10/2022 & 01/2023	$60 \times 5 + 300 \times 45 + 340 \times 4$	0.90 ± 0.13	26.10
i_2 band	10/2022	$60 \times 5 + 204 \times 30$	1.19 ± 0.16	25.05
*NB*515 band	09/2023	240×35	0.83 ± 0.14	24.21

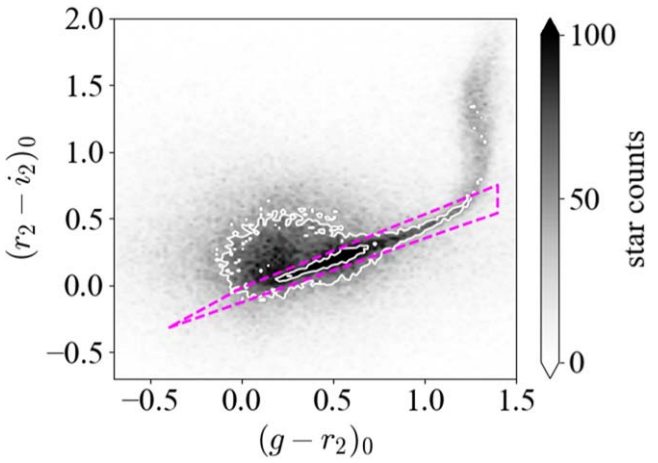

Figure 2. The $(g - r_2)_0$ vs. $(r_2 - i_2)_0$ space of all point sources, which are determined by the `extendedness` parameter of g band. The white contours represent where the star counts are 100 and 200. In the following analysis, we regard the objects within the purple polygon as the "pure" stellar point sources.

Flewelling et al. 2020), stacks each frame, and performs source detection and photometry to create the scientific catalog. After the reduction and calibration, to evaluate the detection completeness, we perform artificial star tests using the hscPipe and `injectStar.py` (Ogami et al. 2024). We follow the same method as in Ogami et al. (2024). Briefly, we embed the artificial stars with given magnitudes into the reduced images using `injectStar.py`, then we conduct the detection and photometry using the hscPipe. The outcome of this test (see Table 1) indicates that our broadband photometry is over 1 mag deeper than that of the previous survey (PAndAS; Ibata et al. 2014; McConnachie et al. 2018).

Based on the Galactic dust extinction (Schlegel et al. 1998; Schlafly et al. 2012), we apply the extinction correction for each source. The extinction-corrected magnitudes for each band are

$$\begin{aligned} g_0 &= g - 3.676 \times E(B-V) \\ r_{2,0} &= r_2 - 2.584 \times E(B-V) \\ i_{2,0} &= i_2 - 1.903 \times E(B-V) \\ NB515_0 &= NB515 - 2.862 \times E(B-V), \end{aligned} \quad (1)$$

where the subscript "$_0$" means the extinction-corrected magnitude. The coefficient of the extinction-corrected magnitude of each band is obtained by the same method as Ogami et al. (2024), which multiplies the interstellar absorption curve of Fitzpatrick (1999) with $R = +3.1$ by the spectral energy distribution of a G-type star ($T_{\rm eff} = 7000$ K, $\log Z = -1$, $\log g = 4.5$) and integrates it using the response curve of each band.

3. Selection of the M33 Halo Stars

3.1. Point Sources

In the hscPipe, the parameter `extendedness`, which determines whether the object is a point source (`extendedness==0`) or an extended source (`extendedness==1`), is constructed for each band. In the following analysis, we mainly use those objects that are determined to be the point sources in g band, because the seeing of the g-band images is the best of all the bands in our study (seeing $\sim 0\farcs5$). However, Aihara et al. (2018b) reported that it is difficult to perform star–galaxy classification using the `extendedness` parameter fainter than 24.5 mag of i band. To overcome this problem, we use the $(g - r_2)_0$ versus $(r_2 - i_2)_0$ diagram to extract "pure" stellar point sources, in addition to the `extendedness` parameter. Figure 2 shows the color–color diagram of the point sources that are determined by the `extendedness` parameter of g band. In this space, it is known that the stellar sequence occupies the region from $(-0.2, -0.2)$ to $(1.3, 0.5)$ (e.g., Krisciunas et al. 1998; Lenz et al. 1998). This sequence bends around $((g - r_2)_0, (r_2 - i_2)_0) \sim (1.3, 0.5)$, because there are the many foreground M- and K-type stars. In this space, there are also unresolved background objects around $((g - r_2)_0, (r_2 - i_2)_0) \sim (0.2, 0.2)$, which deviate from the stellar sequence. These objects are composed of quasars and star-forming galaxies, as confirmed by spectroscopic observations (Ahumada 2020; Lyke et al. 2020). Therefore, in this study, we regard the objects within the purple polygon that is drawn by the dashed lines in Figure 2 as the "pure" stellar point sources. This purple polygon is almost the same as in Suzuki et al. (2024) and covers the PARSEC isochrones (Bressan et al. 2012; Marigo 2017) with $-0.5 < [{\rm Fe/H}] < -2.5$ and 8 Gyr $<$ Age $<$ 13 Gyr. We use these "pure" stellar point sources for the following analysis. Finally, our stellar sample does not include cooler stars (e.g., K- and M-type stars), so our sample is a biased selection. However, this bias is probably fine, because we think that the halo of M33 should be as metal-poor as that of the large galaxies (e.g., the Milky Way).

3.2. RGB and RC Stars in M33

Figure 3(a) shows the color–magnitude diagram (CMD) of all "pure" stellar point sources. In this diagram, we can see the clear RGB sequence from $((g - i_2)_0, i_{2,0}) \sim (2, 21)$ to $(1, 24)$. However, due to the low galactic latitude of M33, foreground dwarf stars can be also seen from $\sim(2, 20)$ to $(2, 24)$ (Galactic disk stars) and from $\sim(0, 21)$ to $(1, 23)$ (Galactic halo substructures; Martin et al. 2014) in this diagram. Due to the overlapping of the foreground contaminants with the M33 RGB stars, it is difficult to separate the M33 halo stars from the foreground stars using only the CMD. To solve this problem, Ogami et al. (2024) introduced the RGB probability, $p_{\rm RGB}$, which is the probability that the star is on the RGB calculated

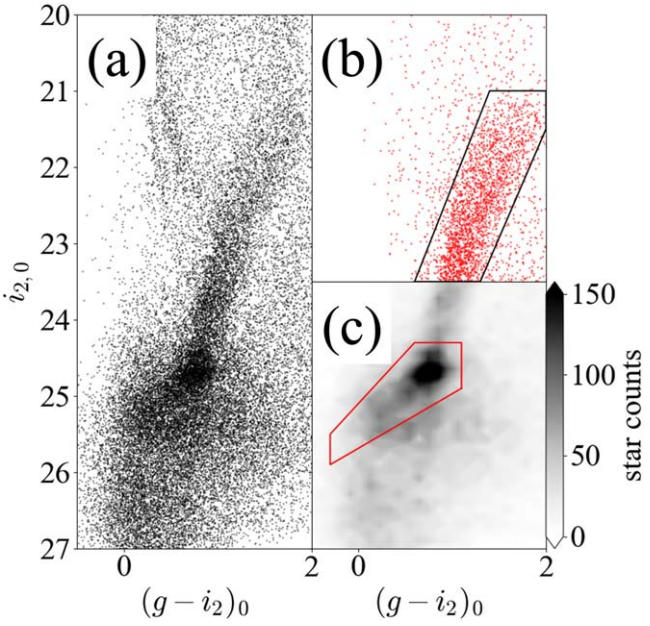

Figure 3. (a) The CMD of the "pure" stellar point sources, which is determined by the $(g - r_2)_0$ vs. $(r_2 - i_2)_0$ space. (b) The CMD of the "pure" stellar point sources with $p_{\rm RGB} > 0.9$. We consider the stars in the black polygon as NRGB stars for our analysis. (c) The same as panel (a), represented by a Hess diagram. We consider the stars in the red polygon as RC stars for our analysis.

by the *NB515* information. Briefly, *NB515* is a narrowband filter covering the MgH band and the Mgb triplet, which are the surface-gravity-sensitive absorption lines, so the dwarf stars and RGB stars are distributed in different loci on the $(NB515 - g)_0$ versus $(g - i_2)_0$ diagram (see Figure 6 in Komiyama et al. 2018). Using this difference on the color–color diagram, Ogami et al. (2024) constructed a probability distribution function of dwarf stars and calculated the dwarf probability and RGB probability based on this information. In addition to the *NB515* information, they also took into account the galactic latitude information in the final RGB probability. However, since the galactic latitude does not change significantly in our observation region, we derive the RGB probability only using the *NB515* information. We calculate $p_{\rm RGB}$ for the stars with $i_{2,0} < 23.5$, and the CMD constructed by the stars with $p_{\rm RGB} > 0.9$ is shown in Figure 3(b). Ogami et al. (2024) reported that even if it was possible for $p_{\rm RGB}$ to remove contamination with ∼90% accuracy, there were a few remaining foreground stars with $(g - i_2)_0 \sim 2.5$. Therefore, we extract the robust RGB stars by selecting stars with $p_{\rm RGB} > 0.9$ and also by selecting stars within the black polygon in Figure 3(b). Ogami et al. (2024) applied the color cut at $(g - i_2)_0 \sim 2.5$, but this study applies the color cut at $(g - i_2)_0 = 2.0$ in the CMD. This is because we have already conducted the color cut for the selection of "pure" point sources at $(g - r_2)_0 \sim 1.5$ (see Section 3.1), so our sample has few stars with $2 < (g - i_2)_0 < 2.5$. In the following analysis, the objects in the black polygon of Figure 3(b) are called *NB515*-selected RGB (NRGB) stars.

Figure 3(c) is the Hess diagram of all "pure" stellar point sources, and we can confirm the overdensity around $i_{2,0} \sim 24.5$. This overdensity corresponds to the RC, assuming a typical distance of M33 (859 kpc; de Grijs et al. 2017). In general, RC stars are known to be more numerous than RGB stars, so RC stars are advantageous for studying low-surface-brightness structures, such as the stellar halo. Therefore, in this study, we consider the "pure" point sources within the red polygon, which covers the PARSEC isochrones with $-0.5 < [{\rm Fe}/{\rm H}] < -2.5$ and $8\,{\rm Gyr} < {\rm Age} < 13\,{\rm Gyr}$, in Figure 3(c) as RC stars. Using these RC stars, we independently probe the stellar halo of M33 and search with NRGB stars. Incidentally, it should be noted that we do not use the *NB515* information to select our RC samples, because RC stars are difficult to separate from foreground dwarf stars in *NB515* color space due to overlapping with the foreground stars.

4. Radial Profile

First, we construct the Hess diagrams for each region using the "pure" point sources defined in Section 3, as shown in Figure 4. The divided area is a region that roughly divides the HSC's field of view into five equal areas. The CMDs in the top row are constructed by "pure" point sources with $p_{\rm RGB} > 0.9$, and those in the bottom row are constructed by "pure" point sources. The boxes for the RGB and RC stars defined in Section 3.2 are also shown in this figure with black and red boxes, confirming that our selected color–magnitude cuts adequately cover the RGB and RC in M33. As seen in these panels, we can confirm the presence of RGB sequences and RC stars beyond 10 kpc from the center of M33. In this section, we construct two types of radial profiles to unravel the information obtained from these Hess diagrams in detail.

4.1. Radial Density Profile

We construct radial density profiles using the NRGB stars and RC stars defined in Section 3 by counting the number of stars in a given region, as follows. First, we limit the analyzed region to $0.^\circ5$ width along the minor axis of the M33 disk ($-0.25 < \eta < 0.25$ in Figure 1). Second, this region is divided into small regions by $0.^\circ2$ along the minor axis of the M33 disk (i.e., the ξ-direction). Third, we count the stars within each divided small region. Then, we take into account the detection completeness. Especially for faint stars, such as RC stars, there is some loss of observational data due to detection completeness. To compensate for this, when we count stars of a given magnitude, we correct for detection completeness in the radial profile, multiplying by the inverse of the detection completeness at that magnitude. Finally, the radial density profile is constructed by dividing the sum of the stellar counts by the area of the region. The constructed profiles of the NRGB stars and RC stars are shown with the black points in Figure 5.

It is known that the limiting magnitude of HSC becomes slightly shallower at the edge of the field of view ($\sim 0.^\circ1$ from the edge; Aihara et al. 2018b). In our data, the 5σ limiting magnitude in each band is also ∼0.05 mag shallower on the periphery. Therefore, to perform a robust analysis, we exclude the innermost and outermost data, which are located at the edges of the field of view, and Figure 5 shows the radial profile after excluding these data points.

To examine the contribution of the disk and halo populations, we fit models to these profiles. We consider a three-component model with an exponential disk, a power-law stellar halo, and a uniform component assuming remaining contamination (foreground stars for the profile of NRGB stars and

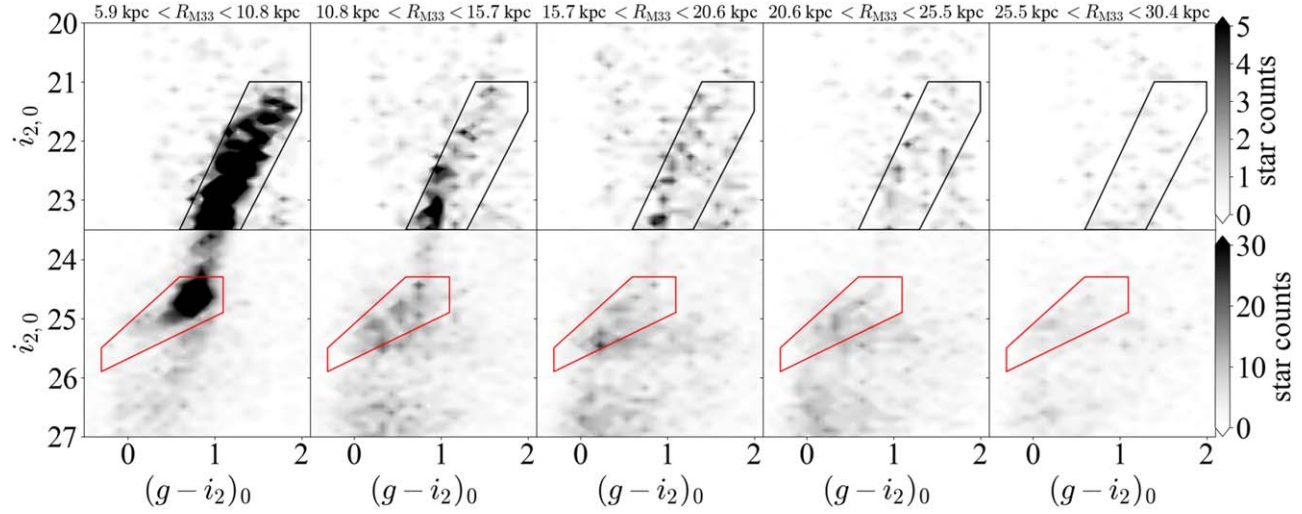

Figure 4. Top row: the Hess diagrams of "pure" stellar point sources with $p_{\rm RGB} > 0.9$. The black polygons show the boundary of the RGB defined in Section 3.2. Bottom row: the Hess diagrams of "pure" point sources. The red polygons show the boundary of the RC defined in Section 3.2. It is noted that the color scale representing the number density is different in the top and bottom rows.

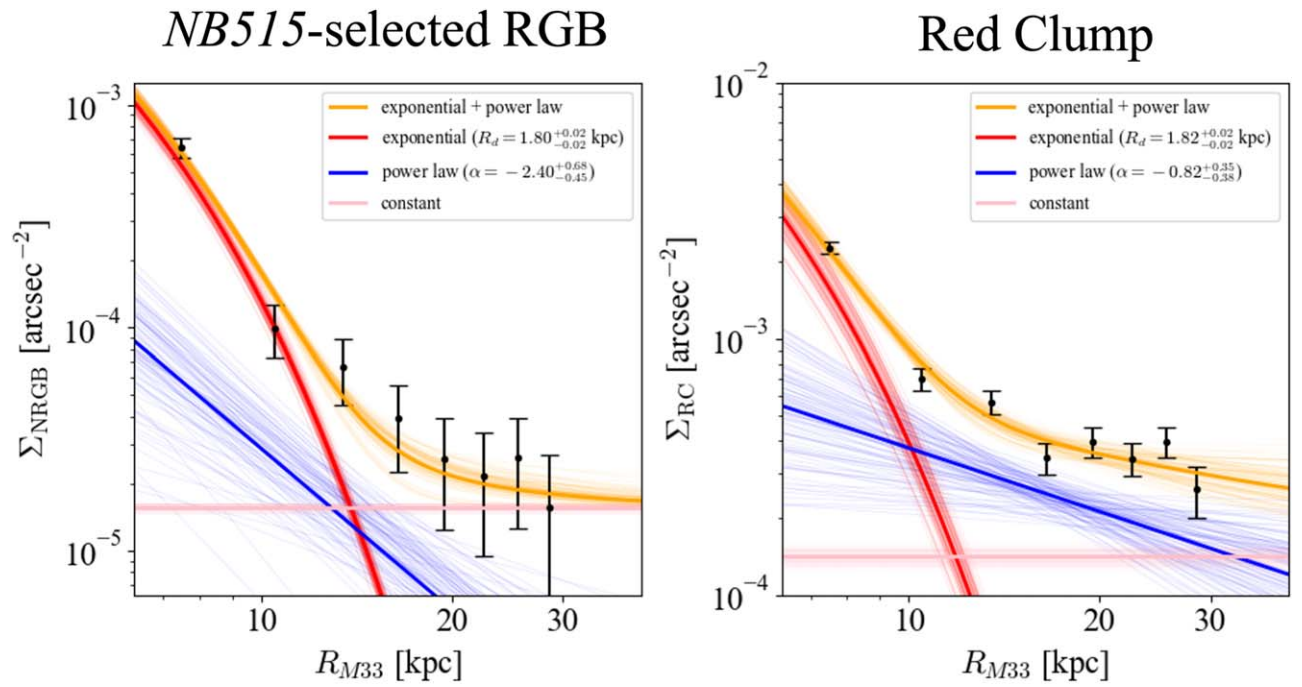

Figure 5. Left: the radial density profile of the NRGB stars. The black dots and their error bars indicate the number density of the stars in each region and their Poisson errors. The orange line shows the MCMC-fitted profile result (halo, disk, plus remaining contamination components). The red, blue, and pink lines are the individual profiles for the disk, halo, and contamination components, respectively, when we assume a prior distribution of R_d as a Gaussian distribution with 1.86 kpc. For each line, the thick line shows the profile using median values of the parameters estimated by MCMC and the thin lines indicate the results of 1000 random samples from the posterior distribution. Right: the same as in the left panel, but the profile is constructed using RC. The constant contamination population is not plotted in this figure, due to its small value.

background galaxies for the profile of RC stars):

$$\Sigma(R) = \Sigma_{\rm disk,0} \exp\left(-\frac{R}{R_d}\right) + \Sigma_{\rm halo,0}\left(\frac{R}{\rm kpc}\right)^{\alpha} + \Sigma_{\rm c}, \quad (2)$$

where R_d is the disk scale length, α is the projected power-law index for the stellar halo, and $\Sigma_{\rm disk,0}$, $\Sigma_{\rm halo,0}$, and $\Sigma_{\rm c}$ are the surface density scale factors for the disk, halo, and contamination, respectively. Based on this equation, we construct a likelihood function to fit the binned radial density profile (see Figure 5):

$$\mathcal{L} = \prod_n \frac{1}{\sqrt{2\pi\sigma_i^2}} \times \exp\left[\frac{-(y_i - \Sigma(R_i|\Sigma_{\rm disk,0}, R_d, \Sigma_{\rm halo,0}, \alpha, \Sigma_{\rm c}))^2}{2\sigma_i^2}\right], \quad (3)$$

where $\Sigma_{\rm disk,0}$, R_d, $\Sigma_{\rm halo,0}$, α, and $\Sigma_{\rm c}$ are the same parameter in Equation (2). R_i and y_i correspond to the radial distance and stellar density of the ith data point of the radial profile shown in

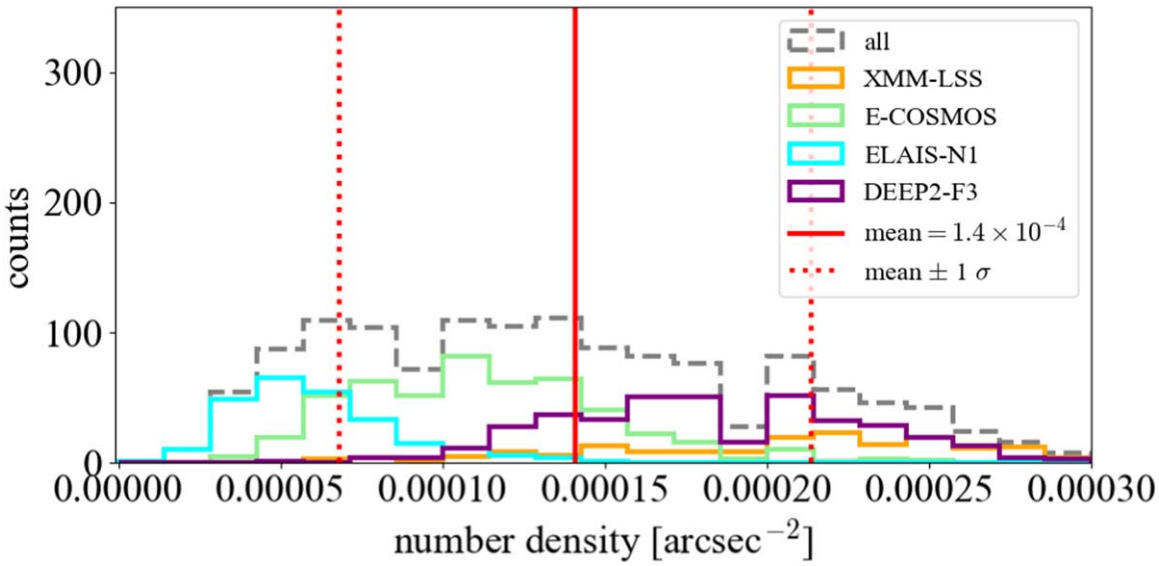

Figure 6. The histogram of the surface number density of remaining background galaxies from the HSC-SSP DEEP data. The gray dashed line shows a histogram using all the data in the HSC-SSP DEEP region, and the solid and dashed red lines are the mean and 1σ values of this histogram. The orange, light green, cyan, and purple lines show histograms for four regions comprising the HSC-SSP DEEP data (XMM-LSS, E-COSMOS, ELAIS-N1, and DEEP2-F3).

Figure 5, respectively. σ_i is the uncertainty of the stellar density. In the case of the profile of the NRGB stars, we use wide and flat prior distributions (i.e., uninformed prior distributions) for $\Sigma_{\rm disk,0}$, $\Sigma_{\rm halo,0}$, α, and $\Sigma_{\rm c}$. It is difficult to estimate the disk properties because our observation region covers the outside of the typical M33 disk. Hence, we adopt a Gaussian distribution with a mean of 1.86 kpc as the disk scale length R_d and its standard deviation of 0.02 kpc, which is the statistical uncertainty of R_d, from Kam et al. (2015), which was estimated by Spitzer/IRAC 3.6 μm data. In addition to an assumed Gaussian distribution with a mean of 1.86 kpc, we adopt a Gaussian distribution with a mean of 4.34 kpc, because the disk scale length of M33 was estimated to be 4.34 kpc in a previous study (Smercina et al. 2023), which detected the stellar halo of M33.

In the case of the RC stars, we also use the same uniform priors as the RGB stars for $\Sigma_{\rm disk,0}$, $\Sigma_{\rm halo,0}$, and α, and the same Gaussian distributions as the RGB stars for R_d. However, for $\Sigma_{\rm c}$, we adopt a Gaussian distribution of the mean and standard deviation values derived from observational data instead of an uninformed prior, because it is possible to use observational data to estimate the contribution from background galaxies. The amount of remaining background galaxies is estimated using data from the HSC-SSP DEEP region (Aihara et al. 2018a). We conduct the same reduction and calibration as for our observational data, and we perform the same color and magnitude cut for the comparison data (i.e., for HSC-SSP DEEP data, we select the objects within the purple polygon in Figure 2 and the red polygon in Figure 3(c)). After that, we count the number of sources for each 0.5×0.2 deg^2 region for these data, correcting their detection completeness. Figure 6 shows the histogram of the number density of the remaining background galaxies from the HSC-SSP DEEP data. HSC-SSP DEEP consists of observations for four different regions. Therefore, Figure 6 shows the distribution of all HSC-SSP DEEP data as the gray dashed lines and the distribution of each region as the orange, light green, cyan, and purple solid lines. From this figure, we find that the surface density of the remaining objects in the HSC-SSP DEEP data has a mean value of 1.4×10^{-4} arcmin^{-2} and a standard deviation of 7.3×10^{-5} arcmin^{-2}, shown as the red solid and dashed lines in Figure 6. We set the Gaussian prior for the parameter $\Sigma_{\rm c}$ using these mean and standard deviation values. From Figure 6, we see that the number of remaining background objects varies from region to region, and the standard deviation is large relative to the mean value. The identification of diffuse structure, such as the stellar halo, is particularly sensitive to the background contamination level, due to the low expected number density of the structure. Therefore, we also fit profiles with fixed $\Sigma_{\rm c}$ (not as a parameter) with the maximum or minimum values obtained from HSC-SSP data.

We perform the Markov Chain Monte Carlo (MCMC) fitting using the Python module `emcee` (Foreman-Mackey et al. 2013) to examine the contribution of the disk and halo populations. We initialize the sampler with 100 walkers, with 10,000 steps after a burn-in period of 100,000 steps, to ensure a good sampling of the posterior distributions. Figure 5 also shows the results of the profile fitting, shown as the thick orange line, and the results of 1000 random samples from the posterior distribution, shown as thin orange lines. This figure shows the fitting results when the prior distribution of R_d is assumed to be a Gaussian distribution with a mean of 1.86 kpc. Figure 7 also shows the fitting results when the prior distribution of R_d is assumed to be a Gaussian distribution with a mean of 4.34 kpc. In both figures, the fitting results for each population are indicated by red lines for the disk, blue lines for the halo, and pink lines for contamination. Table 2 also shows the estimation results for all fitting cases. We show the posterior and marginalized distributions for all fitting cases in the Appendix.

In the case of RC stars, we confirm that the halo population is sensitive to the amount of contamination. Hence, the value of the alpha index is inconsistent, especially for the cases with the highest and lowest amounts of contamination. Besides this, the fitted RC profiles tend to be shallower than the result of the NRGB stars. Taking the statistical error into account, the result of the RC stars with the highest contamination is consistent with the result of the NRGB stars, so it is possible that there is

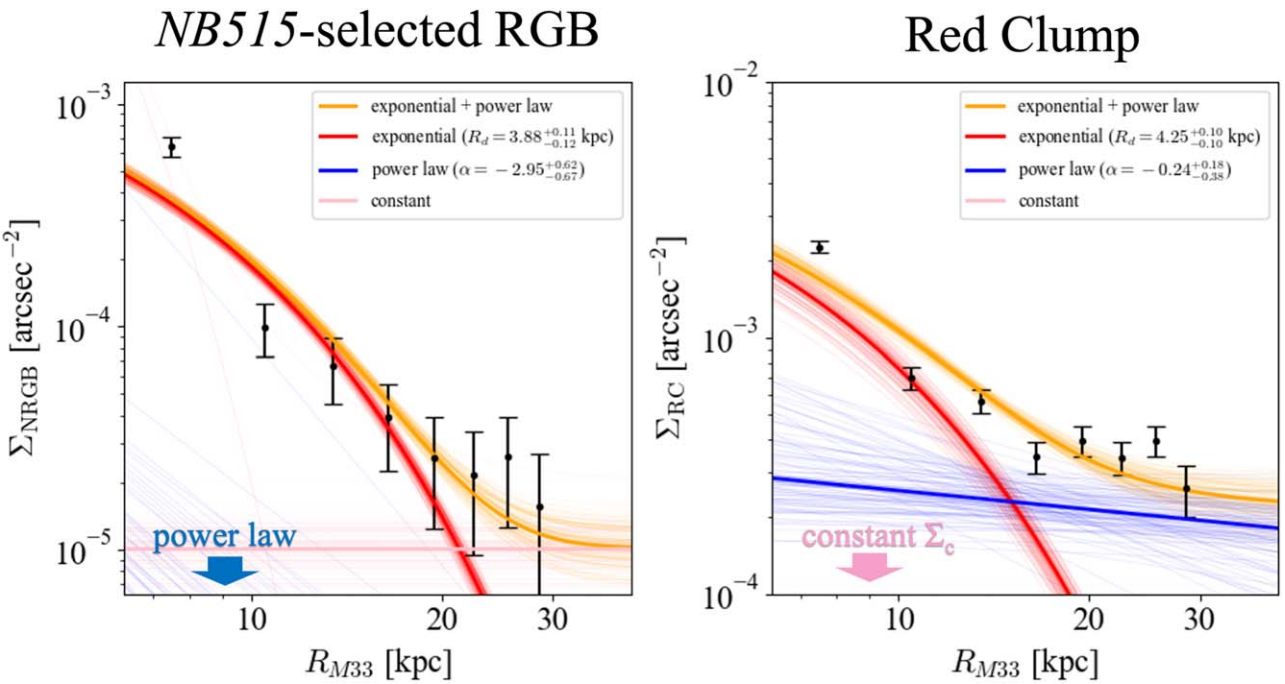

Figure 7. The same as Figure 5, but the assumed prior for R_d is a Gaussian distribution with a mean of 4.34 kpc.

Table 2
The Estimated Results of the Radial Profiles

Case	$\Sigma_{\rm disk,\ 0}$ (arcsec^{-2})	R_d (kpc)	$\Sigma_{\rm halo,\ 0}$ (arcsec^{-2})	α	$\Sigma_{\rm c}$ (arcsec^{-2})
NRGB ($R_d = 1.86$ kpc, Uniform prior)	$0.034^{+0.003}_{-0.003}$	$1.80^{+0.02}_{-0.02}$	$0.007^{+0.014}_{-0.0006}$	$-2.40^{+0.68}_{-0.45}$	$0.0000157^{+0.0000004}_{-0.0000004}$
NRGB ($R_d = 4.34$ kpc, Uniform prior)	$0.0024^{+0.0002}_{-0.0002}$	$3.88^{+0.11}_{-0.11}$	$0.0014^{+0.0008}_{-0.0009}$	$-2.95^{+0.62}_{-0.67}$	$0.000010^{+0.000002}_{-0.000002}$
RC ($R_d = 1.86$ kpc, Gaussian prior)	$0.10^{+0.01}_{-0.01}$	$1.82^{+0.02}_{-0.02}$	$0.0025^{+0.005}_{-0.001}$	$-0.82^{+0.35}_{-0.37}$	$0.00014^{+0.00001}_{-0.00001}$
RC ($R_d = 4.34$ kpc, Gaussian prior)	$0.008^{+0.001}_{-0.001}$	$4.25^{+0.10}_{-0.10}$	$0.002^{+0.003}_{-0.001}$	$-0.92^{+0.61}_{-0.37}$	$0.00014^{+0.0001}_{-0.00001}$
RC ($R_d = 1.86$ kpc, maximum Σ_c)	$0.10^{+0.01}_{-0.01}$	$1.82^{+0.02}_{-0.02}$	$0.04^{+0.03}_{-0.03}$	$-2.2^{+0.5}_{-0.3}$	$(2.9 \times 10^{-4}$; fixed)
RC ($R_d = 4.34$ kpc, maximum Σ_c)	$0.008^{+0.001}_{-0.001}$	$4.22^{+0.01}_{-0.01}$	$0.004^{+0.003}_{-0.003}$	$-2.9^{+0.7}_{-0.7}$	$(2.9 \times 10^{-4}$; fixed)
RC ($R_d = 1.86$ kpc, minimum Σ_c)	$0.10^{+0.01}_{-0.01}$	$1.82^{+0.02}_{-0.02}$	$0.001^{+0.001}_{-0.001}$	$-0.46^{+0.21}_{-0.22}$	$(1.5 \times 10^{-5}$; fixed)
RC ($R_d = 4.34$ kpc, minimum Σ_c)	$0.077^{+0.0007}_{-0.0009}$	$4.34^{+0.02}_{-0.02}$	$0.0004^{+0.0007}_{-0.0002}$	$-0.19^{+0.14}_{-0.31}$	$(1.5 \times 10^{-5}$; fixed)

Note. These values are the median of the posterior distribution and the 68% credible intervals.

still some remaining contamination in our RC sample and we may overestimate the M33 halo stars. It is noted that the RC and NRGB stars may be probing slightly different samples. The NRGB stars are biased toward lower metallicities, due to the color–magnitude cut, while the RC stars tend to be younger or more metal-rich than the NRGB stars, so this difference in population may affect the differences in the results of the radial density profile.

Our result shows the alpha indices of the halo component are shallower than -3, depending on the intensity of the contamination sources. Except for the results in the NRGB cases, and the result in the RC case assuming maximum contamination sources, our estimated values are inconsistent with Smercina et al. (2023), if the stellar halo extends to the outer region with the same power law with $\alpha \sim -3$ that is estimated by Smercina et al. (2023). However, in this study, we analyze the outer region, while the region that Smercina et al. (2023) estimated is the inner region (<5 kpc; see the red polygon in Figure 1). In the Milky Way, the halo profile has a break, and the gradient of the profile changes at the break. Therefore, this result may indicate that the gradient of the stellar halo of M33 changes in the outer region as well; M33 may have double halos (an inner and outer halo). Our results that show the shallower population are discussed in detail in Section 5.1.

4.2. Color Profile

It is known that the color of RGB/RC is sensitive to the age and metallicity of the stellar system. To confirm the differences in spatial gradient of the population in M33, we construct the color profile of NRGB/RC stars. Figure 8 shows the constructed projected radial color profiles. To construct the color profile, we use only stars with $-0.25 < \eta < 0.25$ for simplicity as well as the radial density profile. The top panel indicates the color profile of the NRGB stars that are in the black polygon in Figure 3(b), and the bottom panel shows the color profile of the RC stars that are in the red polygon in Figure 3(c). In this figure, the black dot shows the color of each NRGB/RC sample and the black error bar shows its photometric error.

To examine the color gradient, we perform simple linear regression on this profile using MCMC fitting. We initialize the sampler with 100 walkers, with 10,000 steps after a burn-in

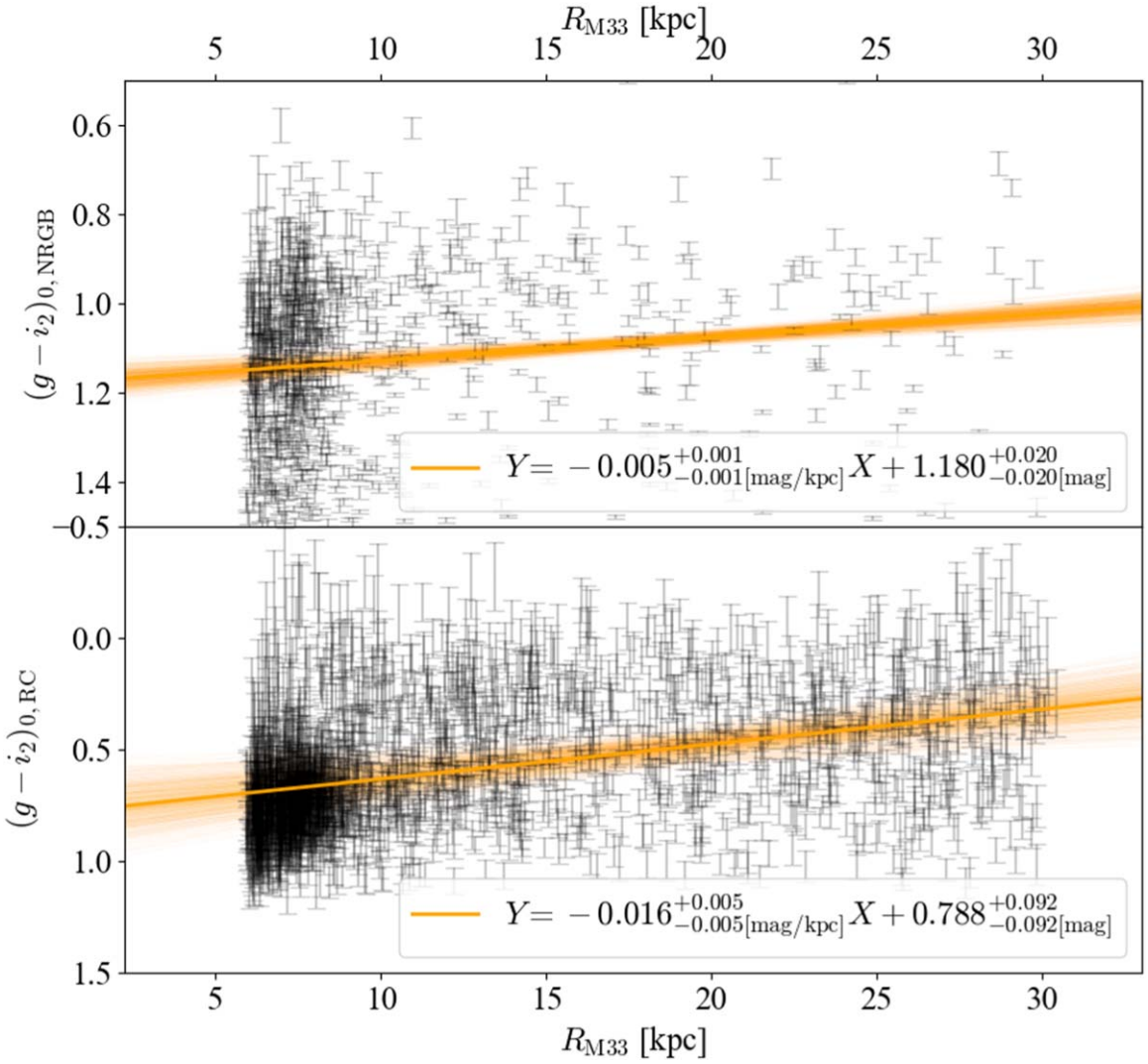

Figure 8. The projected radial color profile. The top panel shows the color profile of the NRGB stars, and the bottom panel shows the color profile of the RC stars. The thick orange line shows the results of linear regression, and the thin orange lines indicate the results of 1000 random samples from the posterior distribution.

period of 100,000 steps, to ensure a good sampling of the posterior distributions. We show the posterior and marginalized distributions in the Appendix. In Figure 8, we show the result using the median value of the posterior distribution estimated by MCMC as the orange thick line. From this result, we confirm the existence of a color gradient in the NRGB/RC stars of M33, suggesting that the outer part of M33 has a more metal-poor and/or older population. In the Milky Way, an age gradient is found to exist in the disk (e.g., Martig et al. 2016). However, our radial density profiles suggest that halo stars are more dominant than disk stars beyond ∼15 kpc (see Figure 5), so the difference in color between the inner and outer regions suggests the presence of an old metal-poor population in the outer region of M33, which is possibly the stellar halo.

In order to investigate this color gradient, we construct normalized color distributions of the RC stars for each region, as shown in Figure 9. Figure 9 shows the normalized color distributions of the RC stars. The divided regions for constructing these distributions are regions that roughly divide the HSC's field of view into five equal areas. In this color distribution, we can visually identify two components at $(g - i_2)_0 \sim 0.2$ and $(g - i_2)_0 \sim 0.7$. To confirm these components, we fit a double-Gaussian model to these distributions. In Figure 9, we show the fitting results as the red and blue lines. In Figure 10, we also show the estimated mean and standard deviation of two components as a function of distance from the center of M33. The color of the plots in Figure 10 corresponds to the color of the lines in Figure 9. From these figures, we can confirm that two Gaussian distributions well reproduce our color distributions, and each population does not change from region to region. Also, it seems that the inner region is contaminated by red stars (i.e., young and/or metal-rich stars) and the outer region is contaminated by blue stars (i.e., old and/or metal-poor stars). Therefore, the color gradient shown in Figure 8 is due to the fact that red stars, which are dominant in the inner region, sharply decrease toward the outer region, and blue stars are dominant in the outer area. Therefore, we think that in the radial density profile of the RC stars, the extended population that is represented by a power law consists of the blue stars (old and/or metal-poor stars).

5. Discussion

5.1. Shallow Stellar Halo

As described in Section 4, M33 has an extended stellar component like a stellar halo, and some radial profiles are

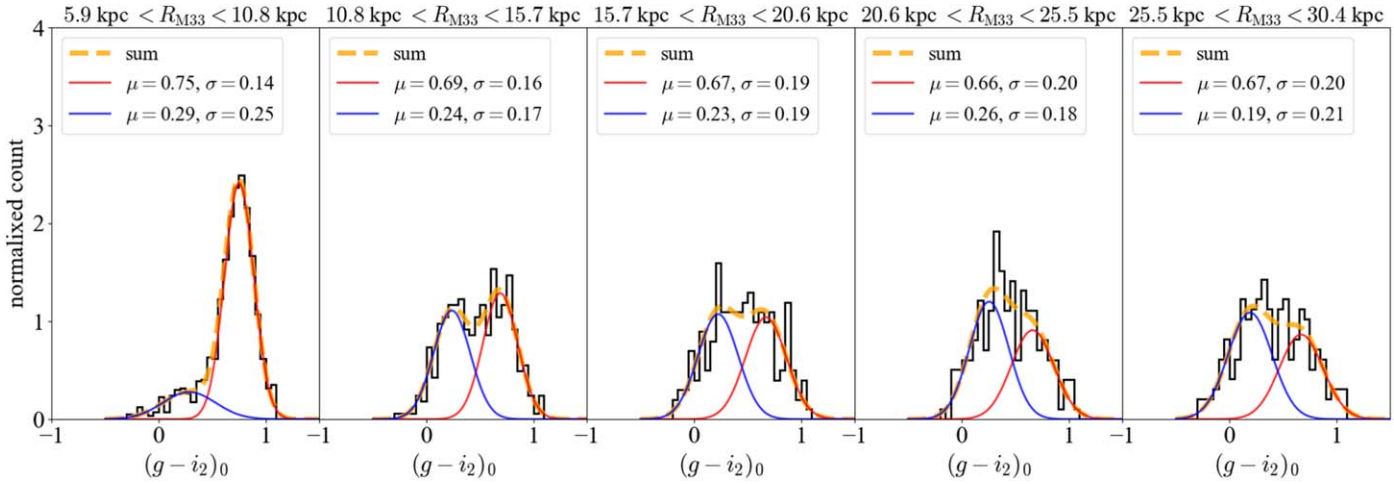

Figure 9. The normalized color distributions of RC stars. The red and blue lines show the fitting results of two Gaussian distributions. The orange dashed line shows the summation of two Gaussian distributions.

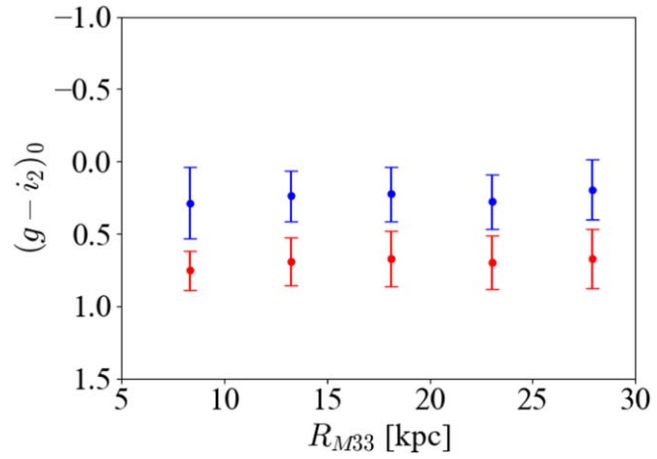

Figure 10. The estimated mean and standard deviation of two Gaussian distributions from our RC stars as a function of distance from the center of M33. The color of these plots corresponds to the color of the lines in Figure 9.

shallow with $\alpha > -3$. Some of our fitted results show a shallow power law, which differ from the result of Smercina et al. (2023). However, this is most likely because they focused on the inner region (<5 kpc) and we focus on the outer region ($5 < R < 30$ kpc), so we may see a different galactic structure.

In the Galactic halo, it is known that the halo is composed of double components: inner/outer halos or in situ/ex situ halos (e.g., Carollo et al. 2007; Deason et al. 2014; Fukushima et al. 2019), which have different alpha indices. Also, the hydrodynamical simulation for galaxy formation by Rodriguez-Gomez et al. (2016) suggests that the simulated stellar halo consists of the in situ and ex situ halos with steep and shallow density slopes, respectively. It is worth noting from their simulation results that the transition radius for these halo components, $r_{\rm trans}$, is about five times a half-light radius for a stellar mass of $10^9\,M_\odot$ (see their Figure 12), i.e., in our case with M33, we obtain $r_{\rm trans} = (5\text{–}7) \times R_d \sim 10\text{–}13$ kpc. Thus, it is possible that the M33 halo has an inner halo at $R < r_{\rm trans}$ with a steep profile of $\alpha \sim -3$ and an outer halo at $R > r_{\rm trans}$ with a shallow slope of $\alpha > -3$ (Figures 5 and 7). In this study, we also perform fitting with a double power law, such as a broken power law, but MCMC does not converge well because there are too many free parameters. To settle this issue, it is expected that future spectroscopic observations (e.g., the Subaru/Prime Focus Spectrograph or PFS; Takada et al. 2014) of the outer regions will confirm whether the halo of M33 is well reproduced by the single halo or double halos.

Our result shows that M33 has a shallow stellar halo in the outer region. However, for the Milky Way, the outer region up to ∼150 kpc was estimated to have $\alpha = -3.74$ for a single power law or −2.92 for a broken power law (Fukushima et al. 2019). Moreover, for M31, the halo profile was estimated to be ranging from −3 to −2 (Ibata et al. 2014). Besides the large spirals in the Local Group, the HST survey also reported that nearby galaxies with stellar halo masses comparable to the Milky Way and M31 (NGC253, NGC891, NGC3031, NGC4565, NGC4945, and NGC 7814) have halo power-law slopes ranging from −5 to −3 (Harmsen et al. 2017). Pillepich et al. (2014) found a strong correlation between stellar halo slope and total halo mass using Illustris simulations. They predicted that the more massive galaxies have shallower stellar halos than the less massive ones. In this simulation result, they suggested that less massive galaxies with halo masses of $\sim 10^{11} M_\odot$ such as M33 have stellar halos reproduced by the power law of $\alpha \sim -5$ (see their Figure 2). However, our results show that M33 has a shallow power-law population, suggesting that M33 may have experienced a unique galactic formation mechanism, if this prediction is correct.

One possible unique scenario for M33 having a shallower population is the M31–M33 interaction. It has been suggested that M33 has interacted with M31 during the past 2–3 Gyr (McConnachie et al. 2009). At this time, the M33 disk is thought to have been extended by tidal forces. If such tidally induced stretching occurred in the disk, the stellar halo may have been extended to form a shallow halo. Considering that a recent study has proposed that M33 is currently in the first infall (Patel et al. 2017), it is necessary to verify the extent to which the halo is extended and to use orbital simulations to probe the extent to which dynamical interactions can stretch the stellar halo to flatten the inferred profile. We emphasize that we need spectroscopic observations (e.g., Subaru/PFS) in the future to verify whether the shallow profile identified in this study is due to a substructure hidden in M33. Besides this, it also needs comparison with other intermediate-mass galaxies (e.g., the Large Magellanic Cloud and Small Magellanic Cloud) to verify whether the shallow profile is unique to

intermediate-mass galaxies or common to spiral galaxies, including large galaxies.

5.2. Halo Properties

Using the radial density profiles in Section 4.1, we estimate the surface brightness of the M33 stellar halo by counting the flux of halo stars for regions up to $\sim 2.2^{\circ}$ ($\sim$30 kpc). Due to the large dispersion of the contamination component for the RC stars (see Figure 6), and for comparison with the large survey observations of M33, which observed only bright RGB stars (PAndAS; McMonigal et al. 2016), we limit ourselves to using the NRGB stars, which are selected based on *NB515* information and color–magnitude information (see Section 3.2), for the derivation of the surface brightness of the M33 halo. If we include the RC stars to derive the surface brightness, the derived value would not change significantly, because the magnitude of our RC samples is $\sim$4 mag deeper (i.e., $\sim$30 times fainter in the units of flux) than the TRGB (see Figure 3). To calculate the surface brightness, we construct the halo fraction profile as a function of distance from the M33 center using the estimated radial density profiles. Then, we count the flux of NRGB stars in each region weighted by the halo fraction. Following this method, we derive the surface brightness for each band. Finally, to compare with the PAndAS study, we convert to the *V*-band surface brightness using the transformation formula (see Equation (8) in Komiyama et al. 2018). The resulting surface brightness is $\mu_V = 35.72 \pm 0.08$ mag arcsec^{-2}. This value is consistent with the upper limit of 35.5 for halo surface brightness suggested in McMonigal et al. (2016). Therefore, it is considered that the robust selection with the narrowband filter allows us to detect the halo structure in this study. The global halo properties will be estimated using new data that are obtained from ongoing observations (I. Ogami et al. 2024, in preparation).

6. Conclusions

We have carried out deep multicolor imaging of the outskirts of M33 using Subaru/HSC. This observation covers a $\sim$1.76 deg^2 field up to $\sim$30 kpc from the center of M33, using the g, r_2, and i_2 bands and *NB515*. We have extracted the point sources using `extendedness` in the hscPipe and the color–color diagram. For RC samples, we have conducted color and magnitude selection. For RGB samples, we have calculated the probability of being an RGB star, in addition to color and magnitude selection. Using these selections, we have succeeded in confirming the clear RGB sequence and RC in the CMD.

To confirm the properties of the outskirts of M33, we have constructed two types of radial profile: a radial density profile for NRGB stars and RC stars, and a radial color profile for RC stars. We have performed model fitting to the radial density profiles and found that M33 has a shallower power-law profile with $\alpha > -3$ than large spiral galaxies and the previous study of M33, in some cases. Based on these results, we can present the following suggestions for the M31 stellar halo. First, regarding the halo profile of M33 being shallow compared to large spirals, it is possible that the M33 halo was influenced by the interaction with M31. As for reconciling our result with previous studies of M33, M33 may have a dual-stellar-halo structure and we might have detected the outer halo of M33 for the first time. In addition, the radial color profile shows that the color of RC stars is bluer toward the outer regions. This result suggests that the old and/or metal-poor population is more dominant in the outer regions, supporting the stellar halo existing beyond 15 kpc.

Finally, we have derived the surface brightness of the stellar halo to compare with the previous study (McMonigal et al. 2016). The surface brightness is $\mu_V = 35.72 \pm 0.08$, and this result is consistent with previous studies. We think that this is caused by the differences in sample selection, and this result shows that our narrowband selection is a powerful tool for probing the low-surface-brightness structure.

Acknowledgments

We acknowledge support in part from MEXT grants-in-aid for Scientific Research (Nos. JP18H05437 and JP21H05448 for M.C., Nos. JP21K13909 and JP23H04009 for K.H., and No. JP22K14076 for T.K.). This work was partially supported by the Overseas Travel Fund for Students (2023) of the Astronomical Science Program, the Graduate University for Advanced Studies, SOKENDAI. Data analysis was in part carried out on the large-scale data analysis system co-operated by the Astronomy Data Center (NAOJ/ADC), Subaru Telescope, NAOJ. E.N.K. acknowledges support from NSF CAREER grant AST-2233781. C.F. and R.F.G.W. are grateful for support through the generosity of Eric and Wendy Schmidt, by recommendation of the Schmidt Futures program.

Facility: Subaru (HSC).

Software: emcee (Foreman-Mackey et al. 2013), astropy (The Astropy Collaboration et al. 2013), Matplotlib (Hunter 2007), numpy (Van Der Walt et al. 2011), corner (Foreman-Mackey 2016).

Appendix
MCMC Results

Here we show the MCMC results as corner plots (posterior distribution and marginal distributions for all parameters) in the case of the radial density profiles (from Figures 11–14) and the radial color profile (Figure 15).

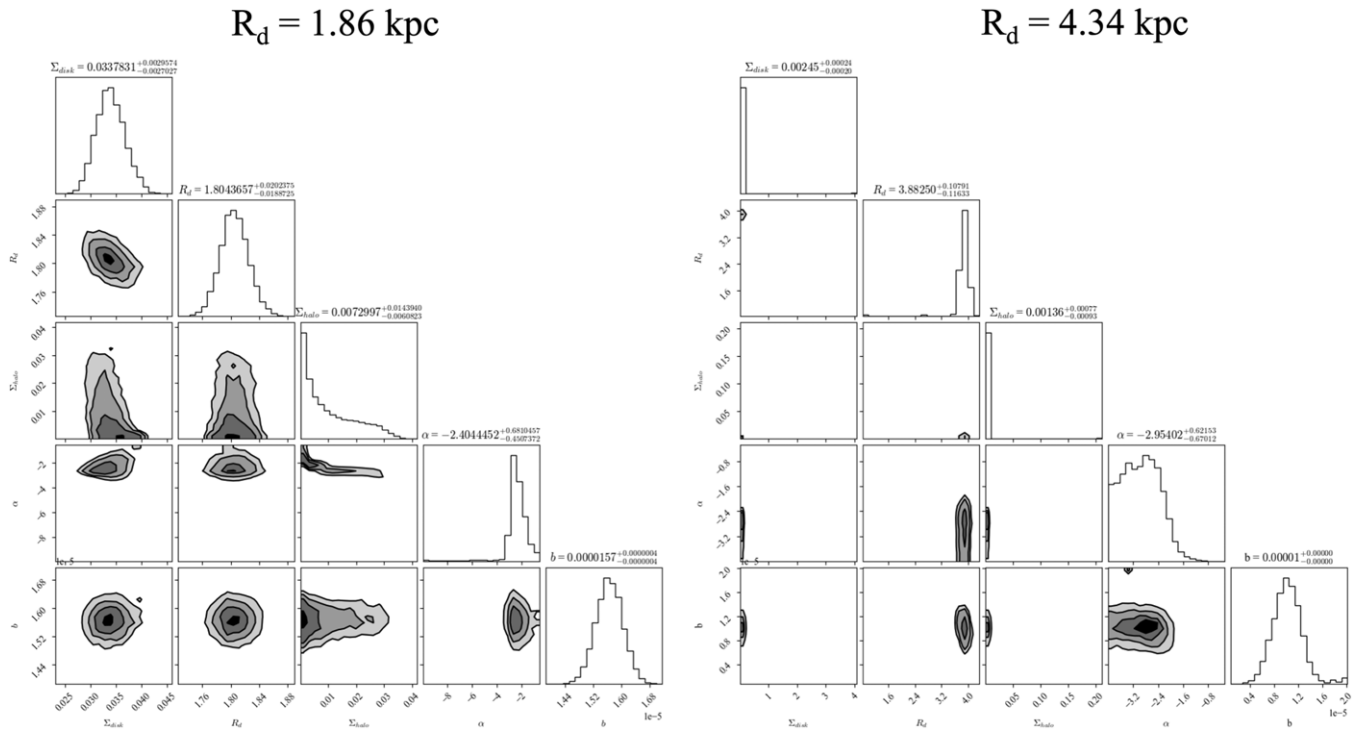

Figure 11. Left: the posterior distributions and marginalized distributions in the radial density profile of NRGB stars, when we assume a prior distribution of R_d as a Gaussian distribution of a mean with 1.86 kpc. Each panel shows the surface density scale of the disk, disk scale radius, surface density scale of the halo, projected power-law index, and contamination scale, from left (top) to right (bottom). Right: the same as in the left panel, but the assumed prior for R_d is a Gaussian distribution with a mean of 4.34 kpc.

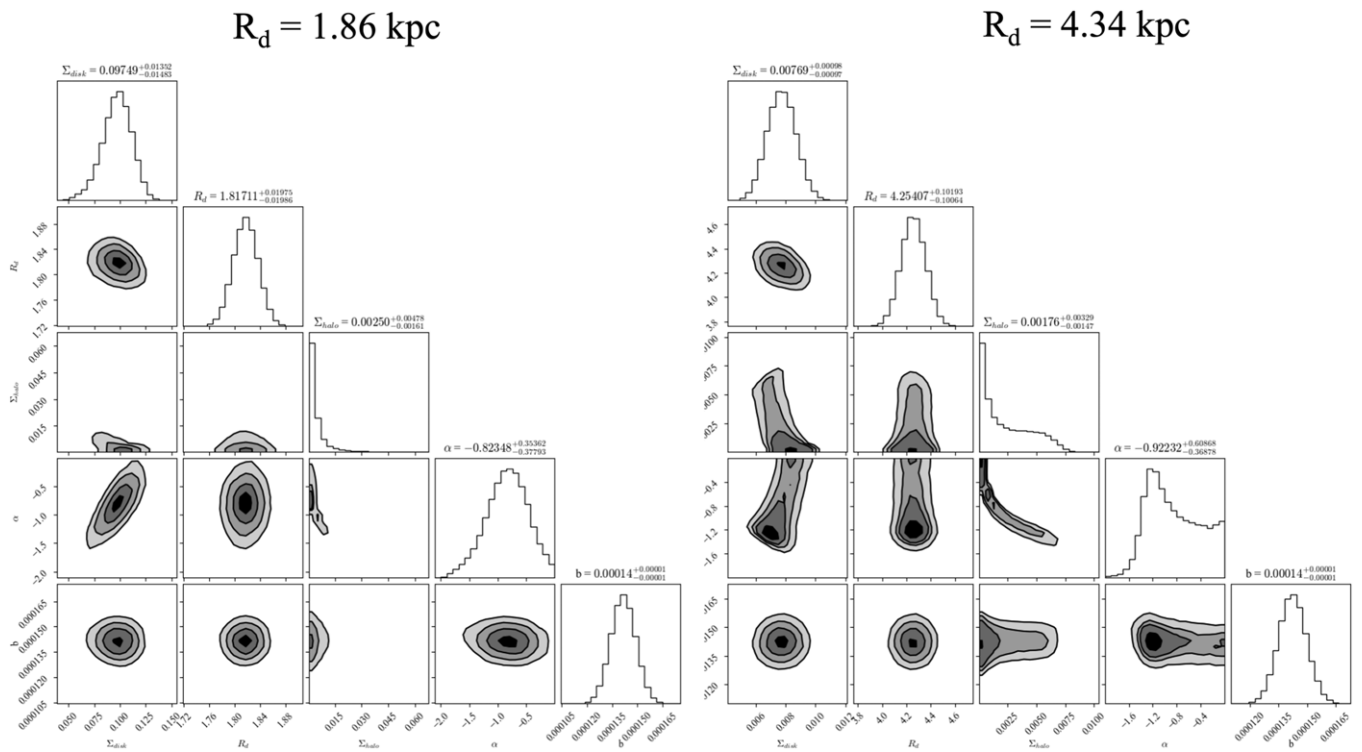

Figure 12. The same as in Figure 11, but for the corner plot from MCMC fitting for the radial density profile of RC using the Gaussian prior with parameters derived from HSC-SSP data.

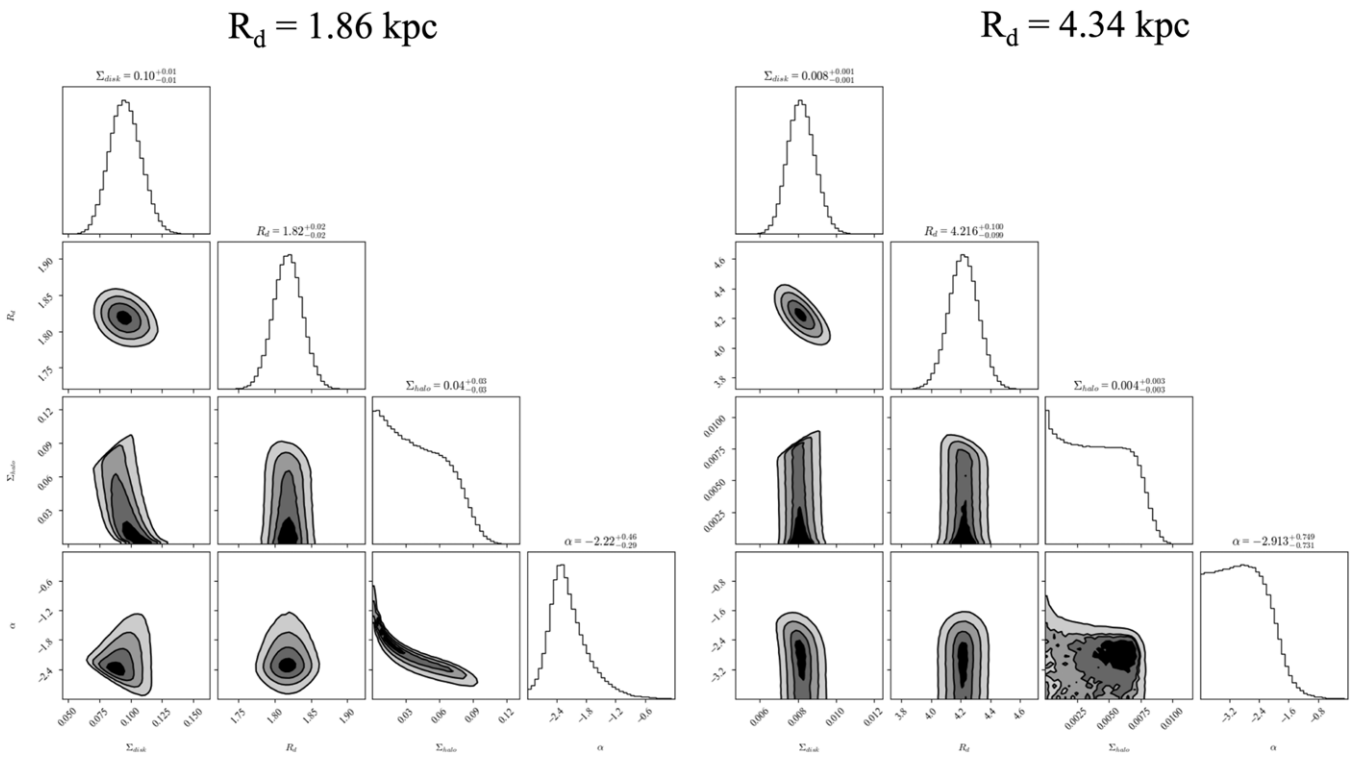

Figure 13. The same as in Figure 11, but for the corner plot from MCMC fitting for the radial density profile of RC using the maximum value of the remaining background galaxies derived from HSC-SSP data.

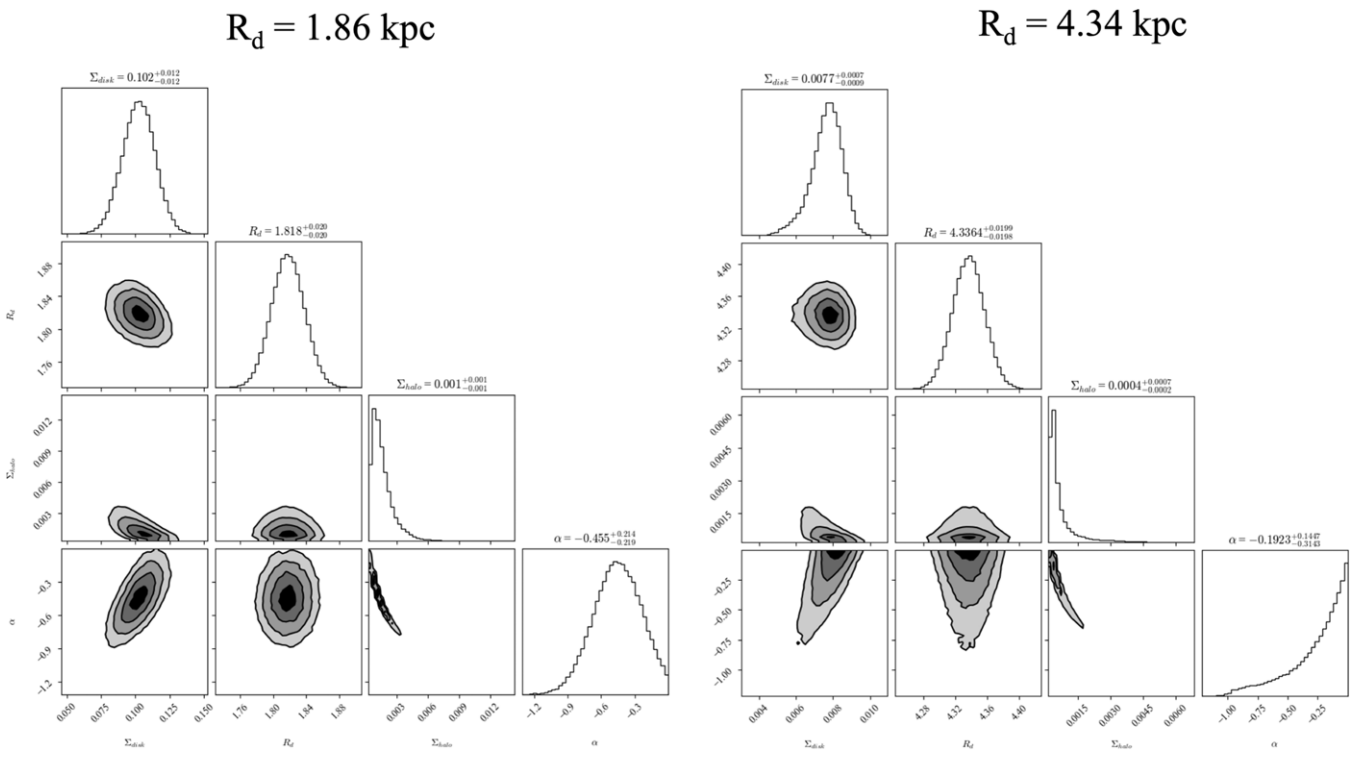

Figure 14. The same as in Figure 11, but for the corner plot from MCMC fitting for the radial density profile of RC using the minimum value of the remaining background galaxies derived from HSC-SSP data.

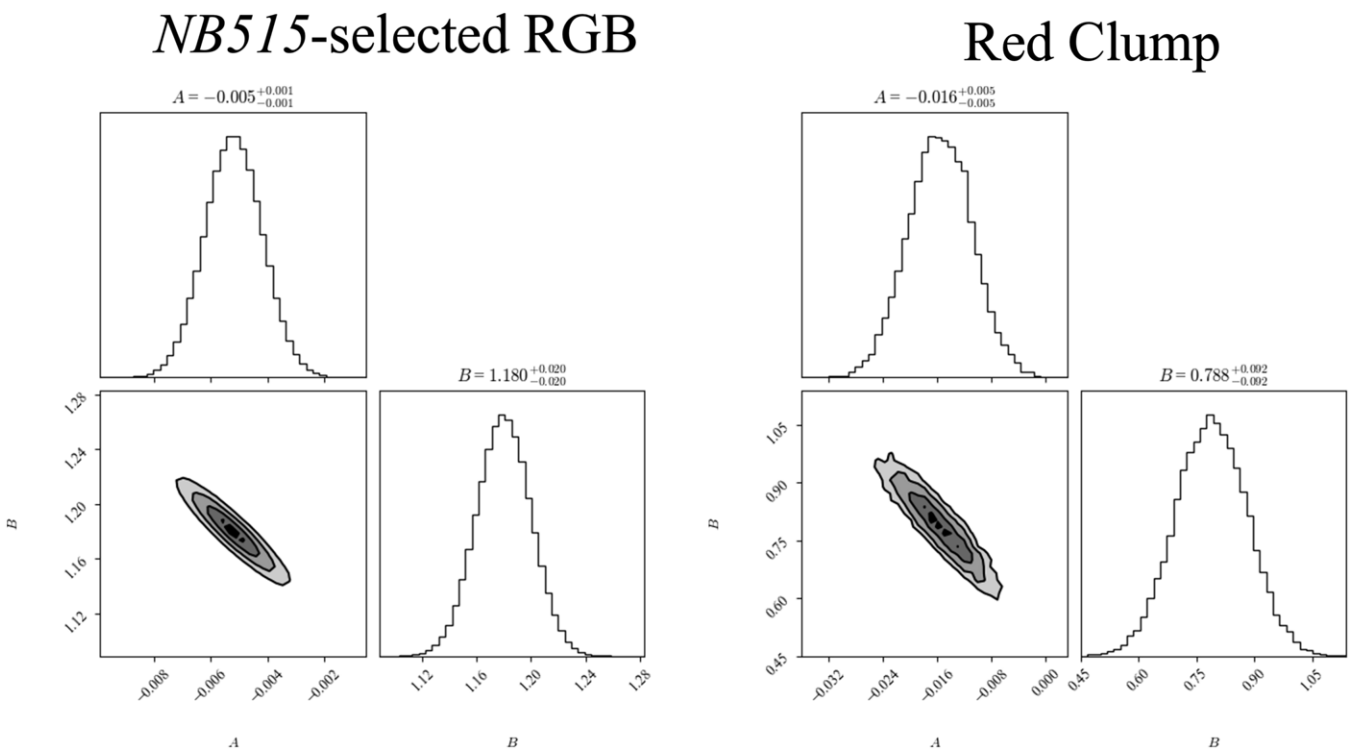

Figure 15. Left: the posterior distributions and marginalized distributions from MCMC fitting for the radial color profile. Each panel shows the color slope of the NRGB stars and the central color scale, from left (top) to right (bottom). Right: the same as in the left panel, but for the corner plot from MCMC fitting for the radial color profile of RC stars.

ORCID iDs

Itsuki Ogami https://orcid.org/0000-0001-8239-4549
Yutaka Komiyama https://orcid.org/0000-0002-3852-6329
Masashi Chiba https://orcid.org/0000-0002-9053-860X
Mikito Tanaka https://orcid.org/0000-0003-2258-7044
Puragra Guhathakurta https://orcid.org/0000-0001-8867-4234
Evan N. Kirby https://orcid.org/0000-0001-6196-5162
Rosemary F. G. Wyse https://orcid.org/0000-0002-4013-1799
Carrie Filion https://orcid.org/0000-0001-5522-5029
Takanobu Kirihara https://orcid.org/0000-0001-6503-8315
Miho N. Ishigaki https://orcid.org/0000-0003-4656-0241
Kohei Hayashi https://orcid.org/0000-0002-8758-8139

References

Abbott, T. M. C., Abdalla, F. B., Allam, S., et al. 2018, ApJS, 239, 18
Aihara, H., Armstrong, R., Bickerton, S., et al. 2018a, PASJ, 70, S8
Aihara, H., Arimoto, N., Armstrong, R., et al. 2018b, PASJ, 70, S4
Ahumada, R., Prieto, C. A., Almeida, A, et al. 2020, ApJS, 249, 3
Behroozi, P., Wechsler, R. H., Hearin, A. P., & Conroy, C. 2019, MNRAS, 488, 3143
Bosch, J., Armstrong, R., Bickerton, S., et al. 2018, PASJ, 70, S5
Bressan, A., Marigo, P., Girardi, L., et al. 2012, MNRAS, 427, 127
Bullock, J. S., & Johnston, K. V. 2005, ApJ, 635, 931
Carollo, D., Beers, T. C., Lee, Y. S., et al. 2007, Natur, 450, 1020
Chambers, K. C., Magnier, E. A., Metcalfe, N., et al. 2016, arXiv:1612.05560
Corbelli, E., Thilker, D., Zibetti, S., Giovanardi, C., & Salucci, P. 2014, A&A, 572, A23
de Grijs, R., Courbin, F., Martínez-Vázquez, C. E., et al. 2017, SSRv, 212, 1743
Deason, A. J., Belokurov, V., Koposov, S. E., & Rockosi, C. M. 2014, ApJ, 794, 115
Fitzpatrick, E. L. 1999, PASP, 111, 63
Flewelling, H. A., Magnier, E. A., Chambers, K. C., et al. 2020, ApJS, 251, 7
Foreman-Mackey, D. 2016, JOSS, 1, 24
Foreman-Mackey, D., Hogg, D. W., Lang, D., & Goodman, J. 2013, PASP, 125, 306
Fukushima, T., Chiba, M., Homma, D., et al. 2018, PASJ, 70, 69
Fukushima, T., Chiba, M., Tanaka, M., et al. 2019, PASJ, 71, 72
Gaia Collaboration, Brown, A. G. A., Vallenari, A., et al. 2016, A&A, 595, A2
Galera-Rosillo, R., Corradi, R. L. M., & Mampaso, A. 2018, A&A, 612, A35
Gilbert, K. M., Guhathakurta, P., Beaton, R. L., et al. 2012, ApJ, 760, 76
Gilbert, K. M., Guhathakurta, P., Kollipara, P., et al. 2009, ApJ, 705, 1275
Gilbert, K. M., Quirk, A. C. N., Guhathakurta, P., et al. 2022, ApJ, 924, 116
Harmsen, B., Monachesi, A., Bell, E. F., et al. 2017, MNRAS, 466, 1491
Homma, D., Chiba, M., Komiyama, Y., et al. 2024, PASJ, 76, 733
Homma, D., Chiba, M., Okamoto, S., et al. 2016, ApJ, 832, 21
Hunter, J. D. 2007, CSE, 9, 90
Ibata, R., Martin, N. F., Irwin, M., et al. 2007, ApJ, 671, 1591
Ibata, R. A., Lewis, G. F., McConnachie, A. W., et al. 2014, ApJ, 780, 128
Ivezic, Z., Axelrod, T., Brandt, W., et al. 2008, SerAJ, 176, 1
Jang, I. S., De Jong, R. S., Holwerda, B. W., et al. 2020, A&A, 637, A8
Jurić, M., Ivezić, Ž., Brooks, A., et al. 2008, ApJ, 673, 864
Kam, Z. S., Carignan, C., Chemin, L., Amram, P., & Epinat, B. 2015, MNRAS, 449, 4048
Komiyama, Y., Chiba, M., Tanaka, M., et al. 2018, ApJ, 853, 29
Krisciunas, K., Margon, B., & Szkody, P. 1998, PASP, 110, 1342
Lenz, D. D., Newberg, J., Rosner, R., Richards, G. T., & Stoughton, C. 1998, ApJS, 119, 121
Lyke, B. W., Higley, A. N., McLane, J. N., et al. 2020, ApJS, 250, 8
Magnier, E. A., Schlafly, E., Finkbeiner, D., et al. 2013, ApJS, 205, 20
Majewski, S. R., Ostheimer, J. C., Kunkel, W. E., & Patterson, R. J. 2000, AJ, 120, 2550
Marigo, P., Girardi, L, Bressan, A, et al. 2017, ApJ, 835, 77
Martig, M., Minchev, I., Ness, M., Fouesneau, M., & Rix, H.-W. 2016, ApJ, 831, 139
Martin, N. F., Ibata, R. A., Rich, R. M., et al. 2014, ApJ, 787, 19
McConnachie, A. W., Ibata, R., Martin, N., et al. 2018, ApJ, 868, 55
McConnachie, A. W., Irwin, M. J., Ibata, R. A., et al. 2009, Natur, 461, 66
McMonigal, B., Lewis, G. F., Brewer, B. J., et al. 2016, MNRAS, 461, 4374
Ogami, I., Tanaka, M., Komiyama, Y., et al. 2024, arXiv:2401.00668
Okamoto, S., Arimoto, N., Ferguson, A. M. N., et al. 2015, ApJ, 809, L1
Patel, E., Besla, G., & Mandel, K. 2017, MNRAS, 468, 3428

Pillepich, A., Vogelsberger, M., Deason, A., et al. 2014, MNRAS, 444, 237
Rodriguez-Gomez, V., Pillepich, A., Sales, L. V., et al. 2016, MNRAS, 458, 2371
Schlafly, E. F., Finkbeiner, D. P., Jurić, M., et al. 2012, ApJ, 756, 158
Schlegel, D. J., Finkbeiner, D. P., & Davis, M. 1998, ApJ, 500, 525
Smercina, A., Dalcanton, J. J., Williams, B. F., et al. 2023, ApJ, 957, 3
Suzuki, Y., Chiba, M., Komiyama, Y., et al. 2024, PASJ, 76, 205
Takada, M., Ellis, R. S., Chiba, M., et al. 2014, PASJ, 66, R1
Tanaka, M., Chiba, M., & Komiyama, Y. 2017, ApJ, 842, 127
The Astropy Collaboration, Robitaille, T. P., Tollerud, E. J., et al. 2013, A&A, 558, A33
Thomas, G. F., McConnachie, A. W., Ibata, R. A., et al. 2018, MNRAS, 481, 5223
Tonry, J. L., Stubbs, C. W., Lykke, K. R., et al. 2012, ApJ, 750, 99
Van Der Marel, R. P., Besla, G., Cox, T. J., Sohn, S. T., & Anderson, J. 2012, ApJ, 753, 9
Van Der Walt, S., Colbert, S. C., & Varoquaux, G. 2011, CSE, 13, 22
Williams, B. F., Durbin, M. J., Dalcanton, J. J., et al. 2021, ApJS, 253, 53
York, D. G., Adelman, J., Anderson, J. E., Jr., et al. 2000, AJ, 120, 1579